Journal of Inorganic and General Chemistry
ZAAC
Zeitschrift für anorganische und allgemeine Chemie

www.zaac.wiley-vch.de

RESEARCH ARTICLE

DOI: 10.1002/zaac.202200281

Site-Preferences in the Mixed-Valent Series $FeMo_{1-n}V_nO_4$: Controlling the Formation of the α-Polymorph and the Charge Localization

Felix L. Osten,[a] Martin Panthöfer,[a] Vadim Ksenofontov,[b] and Angela Möller*[a]

Dedicated to the late Prof. Rudolf Hoppe on the occasion of his 100th birthday

The mixed-valent, solid solution series $FeMo_{1-n}V_nO_4$ ($0 \leq n \leq 0.3$) was synthesized and characterized by x-ray diffraction, and thermal analysis. Assignments of individual Fe-species stem from ^{57}Fe-Mössbauer spectroscopy and DFT-calculations of the electric field gradients. The incorporation of smaller ions (Fe^{III}, V^{V}) represents an internal "chemical pressure" effect stabilizing the low-temperature α-polymorph with increasing n. The site-preference and distribution of vanadium on individual Mo-sites impacts the α→β transition temperatures around 650 K, and causes distinct differences in charge mobility in this hole-doped semiconductor around 225 K. We assign the charge localization in α-$FeMo_{1-n}V_nO_4$ to enhanced electron-phonon coupling within a polaronic scenario.

Introduction

Transition metal molybdates are attractive for environmentally friendly applications in catalysis, electrochemical processes, high-performance supercapacitors, or pressure sensors. In particular $AMoO_4$ (A = Mn, Fe, Co, and Ni) are in the focus of current research activities.[1–8] Aspects like structural transitions, particle size, composites, and mobility of charge carriers are thus of wide interest. Here we concentrate on the structure-property relationships of an iron mixed-valent series, $FeMo_{1-n}V_nO_4$. $FeMoO_4$ exists in two polymorphs at ambient pressure, both crystallizing in the space group (*C*2/*m*, *Z* = 8) and the same set of *Wyckoff* positions.[9–11] The first-order structural phase transitions occur upon cooling from β→α at ≈223 K (−50 °C) and upon heating from α→β around 670 K (400 °C).[6,9,11] The α-polymorph is the low-temperature form. Surprisingly, well above the α→β phase transition ($T_{syn.}$ ≈1000 °C) mainly α-$FeMoO_4$ is obtained directly from the solid state metallothermic redox reaction ($Fe + Fe_2O_3 + 3MoO_3$).[9,12,13] Upon grinding the β-phase is transformed into the low-temperature polymorph at ambient conditions. This places β-$FeMoO_4$ as the high-temperature, low-pressure, and low-density form. Blanco-Guiterrez[6] investigated the pressure sensitivity of β-$FeMoO_4$ ($p_{50\%}$ = 80 bar) and the substitution series ($Fe_{1-x}Mg_xMoO_4$) following a solid solution obeying Vegard's law.[14] They showed that the molar volume decreases linearly with x while $p_{50\%}$ increases to 800 bar for x = 0.8. Hence, the β→α transformation can be induced by smaller cations substituting Fe^{II}. Here, we aim at introducing the smaller Fe^{III} cation into $FeMoO_4$, implementing the redox couple (Fe^{II}/Fe^{III}). To proceed, one has to balance the charge by choosing a trivalent oxo-anion (VO_4^{3-}) to replace MoO_4^{2-}.

To the best of our knowledge, only $FeVO_4$, $Fe(VMoO_7)$, $Fe_4V_2Mo_3O_{20}$, and $Fe_2V_4O_{13}$ are known, exclusively containing Fe^{III} beside V^{V}.[15–19] In a recent high-pressure and DFT study,[20] it was shown that $FeVO_4$-II′ exists above 3.2 GPa (32 kbar) in the α-$MnMoO_4$-type of structure which is isostructural with β-$FeMoO_4$. The molar volume of the ambient modification of $FeVO_4$ ($P\bar{1}$, *Z* = 6) and α-$FeMoO_4$ are almost equal. Thus, we assume that from a structural point of view a substitution series $FeMo_{1-n}V_nO_4$ appears feasible. From thermodynamic arguments, the binary oxides FeO and V_2O_5 do not coexists. It follows that redox reactions prevent the formation of a ternary phase and phase separation should occur.[21] In the case of a solid solution, the entropy gain may account for the existence of mixed-valent $FeMo_{1-n}V_nO_4$. Its experimental realization presents a challenge that we investigated and report on here.

The final point in our consideration is the electronic structure of the semiconductor $FeMoO_4$. Schematically, the density of states (DOS) of the two polymorphs can be described by filled O 2p states at lower energy than the narrow Fe^{II} 3d ($t_{2g}\downarrow^3$, $e_g\downarrow^2$, and $t_{2g}\uparrow^1$) states at the top of the valence band. The

[a] F. L. Osten, Dr. M. Panthöfer, Prof. Dr. A. Möller
Department of Chemistry
Johannes Gutenberg-University Mainz
Duesbergweg 10–14; D-55128 Mainz, Germany
E-mail: angela.moeller@uni-mainz.de
[b] Dr. V. Ksenofontov
Department of Chemistry
Johannes Gutenberg-University Mainz
Duesbergweg 10–14; D-55128 Mainz, Germany
and
Current address:
Max-Planck-Institut für Chemie
(Otto-Hahn-Institut)
Hahn-Meitner-Weg 1
55128 Mainz, Germany

conduction bands are comprised of empty Fe^{II} 3d ($t_{2g}\uparrow^2$ and $e_g\uparrow^2$) and Mo^{VI} 4d-states at higher energy.[8,22,23] The two polymorphs differ due to their contrast in molar density mainly associated with the Mo-O hybridization (covalency), enhancing the dispersion of the respective bands in the case of the α-form. Electrical transport properties have been reported[10,23] and commented on by Goodenough:[22] (i) The extrinsic nature of the electric conductivity in the α-phase, with an activation energy E_a ranging from 0.15 to 0.23 eV, is attributed to a hopping process of minority-spin electrons ($Fe^{II}+Fe^{III}\rightarrow Fe^{III}+Fe^{II}$), which is polaronic in nature and of p-type. The optical energy gaps ($E_g^{\alpha}\approx 1.1$ eV and $E_g^{\beta}\approx 1.7$ eV) relate to the metal to metal charge transfer ($Fe^{II}+Mo^{VI}\rightarrow Fe^{III}+Mo^{V}$).[6]

In comparison, for n-type semi-conducting $FeVO_4$ the activation energy $E_a\approx 0.7$ eV[24] and the direct optical band gap $E_g\approx 2.7$ eV[25,26] are significantly larger. The obvious presence of external defects, e.g. in mechanochemical milled $FeVO_4$ $E_g\approx 2.4$ eV[27] or nano-particles with $E_a\approx 0.3$ eV,[28] renders the respective gaps lower, but not smaller than those for α-$FeMoO_4$. Our conjecture now is that charge-doping of $FeMoO_4$ should be possible, as the activation energy is centered around the minority spin component and within the Fe^{II}/Fe^{III} redox couple of up to $E_a\approx 0.65(5)$ eV observed for iron-battery materials.[29] Replacing Mo^{VI} with V^{V} in $FeMoO_4$ creates a hole in the O2p states, immediately compensated by an electron captured from the Fe^{II}-minority band. This recombination transfers the hole to the latter states at the top of the valence band. In a localized picture, this would correspond to Fe^{III} in a distorted environment. Within a polaronic scenario, coupling to phonons occur and the motion of charge between Fe-sites follows an activated hopping process.[30]

The paper is organized as follows:

- Systematic evaluation of reaction temperatures and corresponding phase fractions of the two $FeMoO_4$ polymorphs and the $FeMo_{1-n}V_nO_4$ series.
- Study of the site preferences of vanadium in $FeMo_{1-n}V_nO_4$.
- Fe^{II}/Fe^{III} distribution and charge localization probed by Mössbauer spectroscopy.

Results and Discussion

The crystal structures of both polymorphs of $FeMoO_4$ contain the Fe_4-butterfly motif consisting of two Fe-sites (Fe1 and Fe2). Molybdate units link all Fe-ions to a 3D-network. Importantly, the two crystallographic sites Mo1 and Mo2 connect differently to the Fe_4-tetramer, see Figure 1. While $[Mo1O_4]^{2-}$ is symmetrically centering a triangular face, $[Mo2O_4]^{2-}$ bridges each edge of the tetramer. The latter results in an asymmetric linking between adjacent individual Fe-sites.

$FeMoO_4$ was synthesized via a metallothermic reduction ($Fe+Fe_2O_3+3MoO_3$). First we address the earlier observations[9,11–13] that the α-polymorph of $FeMoO_4$ is obtained at room temperature despite the fact of a reaction temperature higher than the α→β transition temperature ($T_{\alpha\rightarrow\beta}\approx 400$ °C[9]). Furthermore, it is known that upon grinding the β-form, the transition to α-$FeMoO_4$ occurs well above $T_{\beta\rightarrow\alpha}\approx -50$ °C,[6,11]

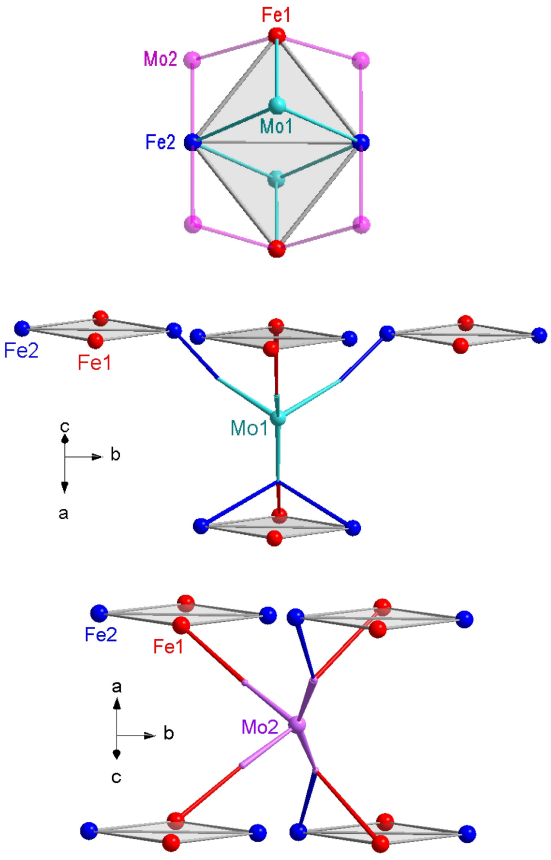

Figure 1. *Top*: Butterfly structural motif (grey shaded) present in both $FeMoO_4$ modifications with the two crystallographic independent Mo-sites. *Middle*: Extended coordination sphere around Mo1 (face-capping). *Bottom*: Extended coordination sphere around Mo2 (edge-connecting). For simplicity, all oxygen atoms are omitted in the graphical representation.

which can be attributed to an external pressure effect. Therefore, we investigated the as-synthesized loose powder samples directly without intermediate grinding by ex-situ x-ray diffraction experiments. Figure 2 shows the dependence of the α- and β-phase ratios for $FeMoO_4$ samples obtained at various reaction temperatures. We observe a linear increase of the α-phase amount with increasing reaction temperature. Below 700 °C no phase pure samples were obtained due to incomplete reactions of the starting materials.

Samples of $FeMo_{1-n}V_nO_4$ (nominal V-substitution, n) were synthesized using the above mentioned metallothermic reduction protocol including respective molar ratios of $FeVO_4$. In order to avoid disproportionation of $FeVO_4$ around 850 °C,[24] we used for this systematic investigation of the V-substituted series the reaction temperature at 800 °C. We recall that at this temperature an initial low α-phase ratio for n = 0 and complete reactions are achieved (Figure 2). Thereby, comparable information on the formation of the α- and β-phase fractions upon increasing V-substitution can be gained. A volume reduction induced by cation and anion substitution within this series relates to the differences in the ionic radii:[31] Fe^{II} ($r_{ion}=0.78$ Å)

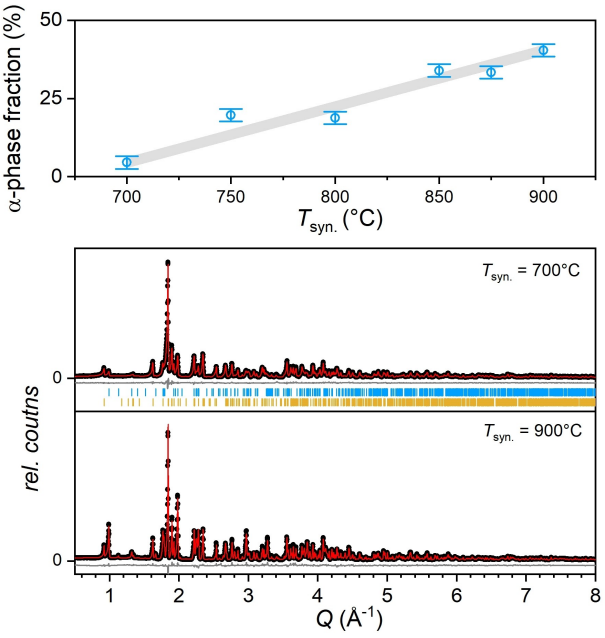

Figure 2. *Top*: Observed α-phase percentage in as-synthesized $FeMoO_4$ at selected reaction temperatures ($T_{syn.}$). *Bottom*: X-ray powder diffractograms for as-synthesized $FeMoO_4$ at 700 °C (R_{wp} = 5.12) and 900 °C (R_{wp} = 6.24). Experimental data (black dots), calculated data (red line), difference (grey line), and Bragg positions referring to the two modifications: α (blue bars) and β (orange bars), respectively.

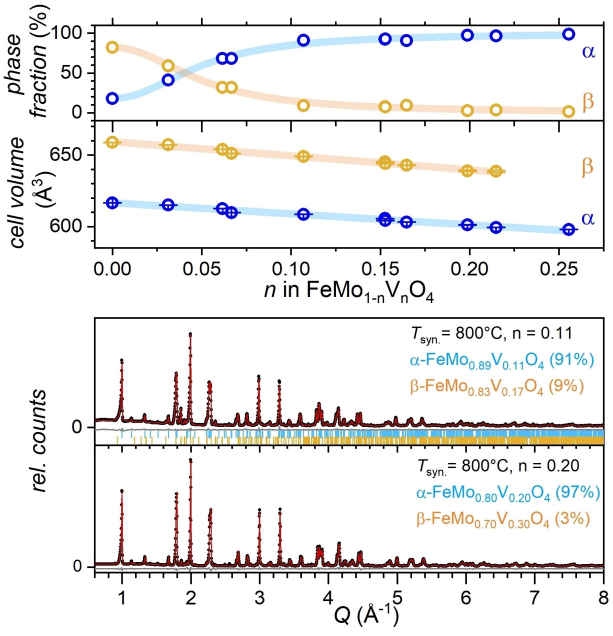

Figure 3. *Top*: Phase percentages and cell volumes for the nominal vanadium substitution in $FeMo_{1-n}V_nO_4$. *Bottom*: X-ray powder diffractograms for as-synthesized $FeMo_{0.89}V_{0.11}O_4$ (R_{wp} = 3.66) and $FeMo_{0.80}V_{0.20}O_4$ (R_{wp} = 5.79). Experimental data (black bullets), calculated data (red line), difference (grey line), and Bragg positions referring to the α- and β-modification given in blue and orange bars, respectively.

replaced by Fe^{III} (r_{ion} = 0.65 Å) and MoO_4^{2-} ($r(Mo^{VI})$ = 0.41 Å) by VO_4^{3-}($r(V^V)$ = 0.36 Å). In a charge-ordered scenario, this should account for a "chemical pressure" effect. Consequently, the α-polymorph with the respective smaller cell volume should be favored.

From Rietveld refinements of x-ray powder diffraction data for $FeMo_{1-n}V_nO_4$, we extracted the phase fractions of the two polymorphs and the cell volumes as a function of the nominal vanadium-substitution (Figure 3). For $n \geq 0.1$ the β-polymorph (β-$FeMo_{1-y}V_yO_4$) amounts to less than 10% and vanishes above $n \approx 0.2$, while the V-substitution in the dominating α-phase (α-$FeMo_{1-x}V_xO_4$) agrees well with the nominal value throughout. The dependence of the cell volume on n has been fitted to a Vegard law[14] with a slope (dV/dn) of −77(3) and −98(4) Å^3/n for the α- and β-phase, respectively. Beyond a nominal 25% V-substitution, we observe decomposition into yet unknown side products. The phase stability range of the substitution series extents up to $x \approx 0.25$ (α-$FeMo_{1-x}V_xO_4$) and $y \approx 0.3$ (β-$FeMo_{1-y}V_yO_4$) for all products crystallizing in the isomorphous $FeMoO_4$ structure types (Figure 4).

From Rietveld refinements of the crystallographic site occupancies (Mo, V) we extracted the following information:

- V-substitution occurs mainly on the Mo1-site (face-capping the Fe_4-tetramer, see Figure 1).
- In the β-phase, the Mo2-site remains unsubstituted.
- The Mo2-site (edge-connecting, see Figure 1) starts to incorporate vanadium above $x \approx 1/8$ in the α-phase.

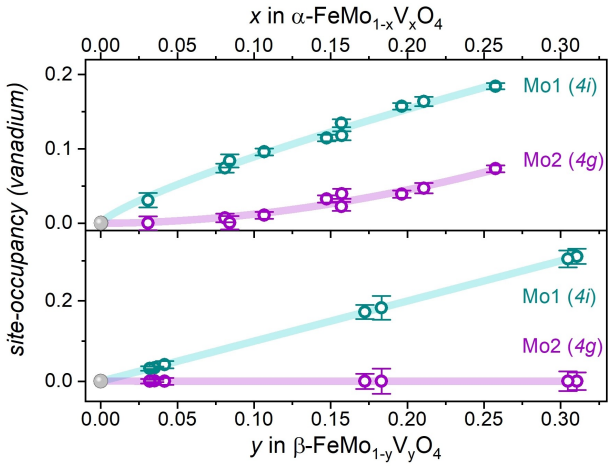

Figure 4. Site occupancy with vanadium on the respective Mo-sites for α-$FeMo_{1-x}V_xO_4$ and β-$FeMo_{1-y}V_yO_4$ in the as-synthesized samples ($FeMo_{1-n}V_nO_4$).

The observation that the vanadium-substitution on the Mo2-site is exclusive for α-$FeMo_{1-x}V_xO_4$ supports the vanishing amount of the β-phase for the as-synthesized compounds with larger n.

Next, we comment on the α→β transition which we investigated by *in-situ* x-ray diffraction and thermal analysis under inert conditions (Figure 5). Both methods reveal that the

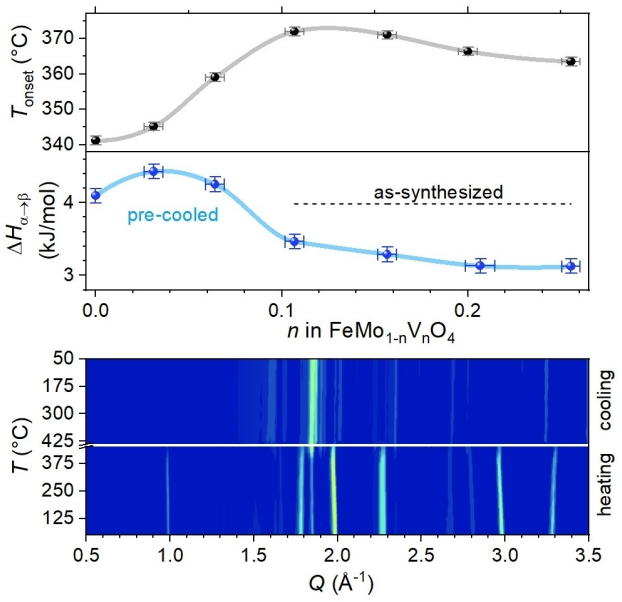

Figure 5. Onset temperatures of the α→β phase transition (top panel) and enthalpies (middle panel) obtained from DSC measurements for the as-synthesized and pre-cooled $FeMo_{1-n}V_nO_4$ series. *Bottom*: Contour plot ($I(Q)\cdot Q$ in counts$\cdot s^{-1}\cdot Å^{-1}$) for a high-temperature x-ray diffraction experiment on $FeMo_{0.89}V_{0.11}O_4$ upon heating and consecutive cooling.

onset transition temperatures ($T_{\alpha\to\beta}$) increase with n. From DSC-measurements we obtain the onset temperatures in the range from 340° to 375 °C. The temperatures at T_{max} of the thermal effect are ≈25 °C higher and in reasonable agreement with the literature: 400 °C[9] and 377 °C.[12] The slight decrease of $T_{\alpha\to\beta}$ for $n \geq 0.1$ might be associated with the V-substitution on Mo2-sites and a 90%+ α-phase contribution of the samples. The total enthalpy ($\Delta H_{\alpha\to\beta}$) measured for the as-synthesized samples reflects the α-$FeMo_{1-x}V_xO_4$ fractions only and yields an average value around 3.9 kJ/mol above $n \approx x \approx 0.1$ in reasonable agreement with pure α-$FeMoO_4$. Interestingly, the pre-cooled samples deviate from this value. Cooling the samples multiple times to liquid nitrogen transforms all β- into α-phases, explicitly β- to α-$FeMo_{1-y}V_yO_4$. For $n < 0.1$ a larger fraction of the latter compound is present and $\Delta H_{\alpha\to\beta}$ increases slightly. For larger substitutions, namely samples containing more than 90% of the α-$FeMo_{1-x}V_xO_4$ phase and only minor amounts of α-$FeMo_{1-y}V_yO_4$, $\Delta H_{\alpha\to\beta}$ is reduced by almost 0.9 kJ/mol. These observations can be understood in terms of (i) size effects, (ii) entropy gain in a solid solution, and (iii) reduced activation energy to change the second coordination sphere of Mo^{VI}, namely C.N.4+2. The latter is probably the most important contribution since the more common coordination number of V^V is four. A comparison with the literature further corroborates the size effect in $AMoO_4$. While $T_{\alpha\to\beta}$ increases with smaller cations (A=Co (500 °C) and Ni (700 °C); $\Delta H_{\alpha\to\beta}$ decreases from 3.6 to 2.5 kJ/mol.[6,9,12] Consecutive heating/cooling cycles reveal no further thermal effects, indicating that all heat associated with the phase transition to the respective β-phases evolves during the initial heating.

In-situ high-temperature x-ray diffraction experiments place the α→β phase transition at $T_{\alpha\to\beta} \approx 375$ °C for $FeMo_{0.89}V_{0.11}O_4$ with x=0.11 (90%, α) and y=0.17 (10%, β), see Figure 5 bottom. The pre-transitional displacement of oxide ions in the α-phase is revealed by the diverging, strong temperature dependent shift of the reflections around 2.9 Å^{-1} and 3.3 Å^{-1}. This is in contrast to the β-phase, which exhibits only minor thermal expansion behavior upon heating and cooling. It should be emphasized that β-$FeMo_{1-n}V_nO_4$ arising from reheating the as-synthesized samples is a mixture, which contains the original β-$FeMo_{1-y}V_yO_4$ and the transformed β-$FeMo_{1-x}V_xO_4$ phases. The latter originates from α-$FeMo_{1-x}V_xO_4$.

Charge localization versus delocalization. The question arises whether a Mo/V-order influences a charge localization on Fe-sites. We recall that the dominant phase upon V-substitution is the α-polymorph with distinct site-preferences on Mo1-positions. Therefore, we focus in this section on the structural data for α-$FeMo_{1-x}V_xO_4$. For x=0.11 and x=0.20 we calculated the Madelung Part of the Lattice Energy (MAPLE)[32] using the effective charge for the V-substituted Mo-sites and the balanced charge values on the Fe-sites. In Table 1 the charge based potentials for the cations are listed. While the charge localization for the Mo/V sites result in almost equal individual site potentials, significant differences are observed for Fe1 and Fe2. The potential gradient is largest for the charge localization at Fe2-sites and minimized for Fe1. Hence, support for the preference of Fe^{III} occupancy on Fe1-sites results. However, no complete charge localization can be expected from this static picture since a potential gradient persist. It should be noted, that the average Fe–O distances are almost equal for α-$FeMo_{0.89}V_{0.11}O_4$ (d_{Fe-O} = 2.11 Å, MEFIR 0.718 Å). The slightly smaller Fe–O^{av} distance of 2.09 Å with a 1% difference in the MEFIR-values for Fe1 and Fe2 marks the small distortion arising from the additional vanadium substitution on Mo2-sites (edge-connecting) in the case of α-$FeMo_{0.80}V_{0.20}O_4$.

DFT-calculations[33,34] were performed for ordered superstructures based on the room-temperature crystal structure of α-$FeMo_{0.89}V_{0.11}O_4$ (*C*2/*m*). The model relates to α-$FeMo_{0.875}V_{0.125}O_4$ with an idealized 1/8 V-substitution on (i) Mo1-sites (*Pm*; *a*, 2*b*, *c*), and (ii) Mo2-sites (*P*2; *a*, 2*b*, *c*), see Figure 1. In these two

Table 1. Site potentials for $FeMo_{1-n}V_nO_4$ obtained from MAPLE-calculations for charge balanced cases on individual Fe-sites.

Site	Charge[a]	Potential[a]	Charge[b]	Potential[b]
Fe1 (n=0.11)	+2.22	−1.92	+2.00	−1.83
Fe2 (n=0.11)	+2.00	−1.98	+2.22	−2.06
Mo1 (n=0.11)	+5.78	−4.09	+5.78	−4.08
Mo2 (n=0.11)	+6.00	−3.95	+6.00	−3.98
Fe1 (n=0.20)	+2.39	−2.02	+2.00	−1.85
Fe2 (n=0.20)	+2.00	−2.02	+2.39	−2.18
Mo1 (n=0.20)	+5.69	−4.04	+5.69	−4.01
Mo2 (n=0.20)	+5.92	−3.93	+5.92	−4.00

[a] Charge localization on Fe1-site. [b] Charge localization on Fe2-site.

scenarios, a V-substituted Fe_4-tetramer is solely surrounded by unperturbed tetramers. Interestingly, the almost equal Mullikan charges for all Fe-sites ($\approx$0.80 *e*) and Mo-sites ($\approx$1.52 *e*) are computed, whereas for vanadium 1.19 *e* is obtained. Importantly, the electric field gradients (EFG) differ for Fe1 and Fe2. The electronic configuration at the iron sites depends on the local anisotropy and charge gradients. The respective EFG's account for these differences at the individual Fe-sites. Experimentally, the quadrupole splitting (QS) is one parameter to reveal such local environments for distinguishable Fe-species. From DFT methods the asymmetry parameters (η) can be obtained and used to calculate the individual QS-values according to Eq. 1:

$$QS = \frac{1}{2} \cdot (1 - \gamma_\infty) \cdot eQ \cdot V_{zz} \cdot \sqrt{1 + \eta^2/3} \quad (1)$$

where $\eta = (V_{xx} - V_{yy})/V_{zz}$), γ_∞ the Sternheimer antishielding factor, *e* the elementary charge and *Q* the nuclear quadrupole moment.[35,36]

Similar to α-$FeMoO_4$ all calculated QS-values equal $-1.45(5)$ mm/s for Fe2-sites, see also Table 2. For Fe1 lower QS-values of $-0.72(6)$ mm/s are obtained from our calculations. This is a remarkable outcome, as it places the Fe1-site in α-$FeMo_{1-n}V_nO_4$ comparable to Fe1 in β-$FeMoO_4$.[11] Since the sign of QS cannot be obtained from paramagnetic Mössbauer spectra, we proceed with $|QS|$-values.

^{57}Fe-Mössbauer spectra for all compounds of the Fe-$Mo_{1-n}V_nO_4$ series were recorded at room temperature under the magic angle in the velocity range from -10 to 10 mm/s in order to probe for pure samples. Impurities such as binary (magnetic) iron-oxides, iron metal, or $FeVO_4$ are absent for the reported $FeMo_{1-n}V_nO_4$ samples, e.g. below the detection limit of this very sensitive method. Here we present the two cases with n = 0.11 and n = 0.20 in detail. The temperature dependent Mössbauer spectra recorded with increasing temperature were fitted by Lorentzian line shape analysis.[37] The hyperfine parameters and site occupancies are given along with the representative spectra in Figure 6 and 7. We recall that the two selected samples contain mainly the α-polymorph (n$\approx$x) and differ only in the preferred site occupancy of vanadium on Mo-sites. For x = 0.11 only the Mo1-position is occupied. The x = 0.20 sample differs due to the additional occupancy on Mo2-sites resulting in a further distortion. In Table 2 we compare the hyperfine parameters for individual sites with literature data for $FeMoO_4$.[11] In general, the chemical shift indicates the oxidation state of iron. Typically, the room temperature values are CS(Fe^{II}) $\approx$ 1.10 mm/s and CS(Fe^{III}) $\approx$ 0.40 mm/s in molybdates.[11,38]

Table 2. Chemical shift (CS) and quadrupole splitting (QS) in mm/s, obtained from fits of Mössbauer spectra at room temperature and 200 K (italic) for $FeMoO_4$ (literature data) and α-$FeMo_{1-x}V_xO_4$ (labelling of individual species according to Figure 6 and 7, see text).

Site	CS	|QS|	Site	CS	|QS|
Fe1[a]	1.04(1)	1.48(2)	**Fe1**[b]	1.13(1)	0.85(1)
Fe2[a]	1.04(1)	1.48(2)	**Fe2**[b]	1.12(1)	2.55(1)
D1a[c]	1.02(1)	1.43(1)	**D1b**[d]	0.99(1)	1.35(3)
D2a[c]	–	–	**D2b**[d]	0.98(1)	1.66(2)
	1.13(1)	*1.86(2)*		*1.04(1)*	*2.00(2)*
Sa[c]	0.38(3)	0	**Sb**[d]	0.35(1)	0
	–	–	**D3b**[d]	*0.38(1)*	*0.21(2)*
D3a[c]	0.77(3)	1.09(5)	**D4b**[d]	1.10(2)	0.50(2)
	0.58(3)	*0.94(5)*		*1.21(2)*	*0.75(2)*

[a] α-modification.[11] [b] β-modification.[11] [c] x = 0.11. [d] x = 0.20.

First, we discuss the hyperfine parameters obtained for $FeMo_{0.89}V_{0.11}O_4$ presented in Figure 6. Four distinguishable iron-species exist with different contributions to the total spectra. The CS-parameters of the two sub-spectra (D1a, blue and D2a, purple) are virtually identical and are assigned to Fe^{II} in the α-phase (see Table 2 for comparison). The much lower CS around 0.38 mm/s of the singlet (Sa, red) identifies the presence of Fe^{III}. The doublet (D3a, yellow) reveals the $Fe^{2+\delta}$ species with an anomalous temperature dependence of CS and QS, clearly dissimilar to the Fe-species mentioned above in typical, localized oxidation states. Thus, we take this feature as an indicator for charge delocalization at temperatures above 225 K and a gradual charge ordering (self-trapping) below. Interestingly, the transition temperature coincides with the $\beta \rightarrow \alpha$ structural transition temperature upon cooling, which is unexpected since the $FeMo_{0.89}V_{0.11}O_4$ sample already contains only the α-polymorph. From Raman spectroscopic measurements, conducted in heating mode, a softening of modes starting

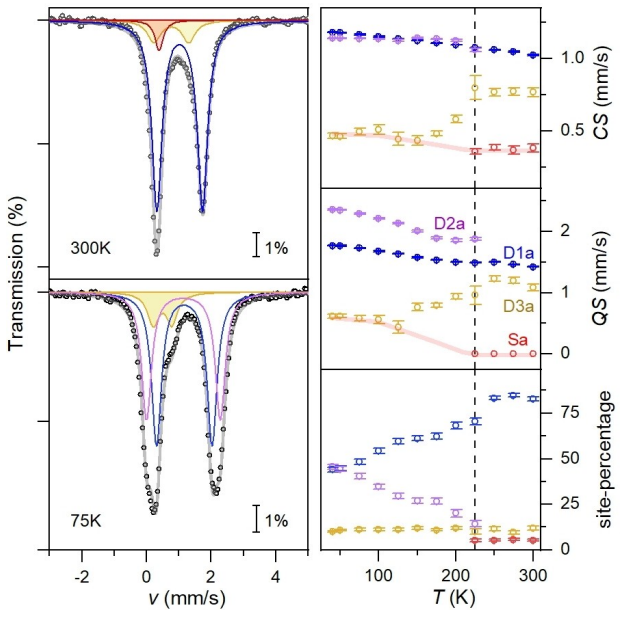

Figure 6. *Left*: ^{57}Fe-Mössbauer spectra for $FeMo_{0.89}V_{0.11}O_4$ at 300 K and 75 K with individual spectral contributions obtained from Lorentzian line-shape analysis. Black circles represent experimental data and grey lines the total fitted spectra. *Right*: Fitted hyperfine parameters for $FeMo_{0.89}V_{0.11}O_4$. The color-coding represents the assignment to different local Fe-sites, see text and Table 2. The dashed line indicates the crossover temperature and the red shaded line serves as a guide to the eye.

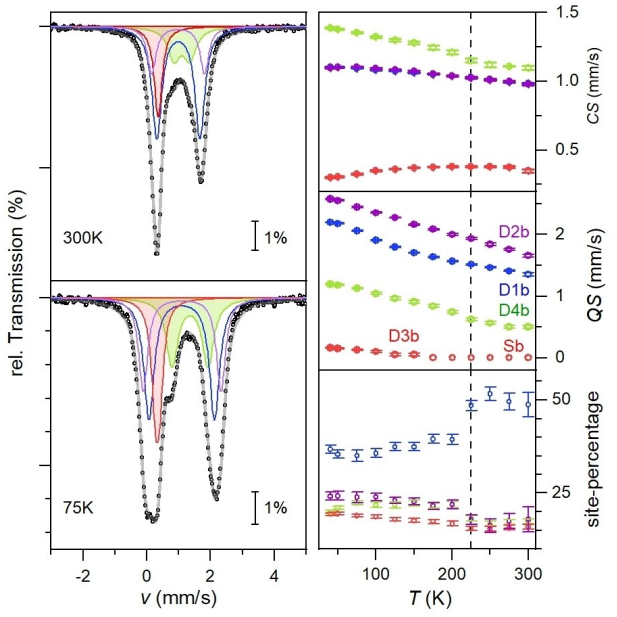

Figure 7. *Left*: ^{57}Fe-Mössbauer spectra for $FeMo_{0.80}V_{0.20}O_4$ at 300 K and 75 K with individual spectral contributions obtained from Lorentzian line-shape analysis. Black circles represent experimental data and grey lines the total fitted spectra. *Right*: Fitted hyperfine parameters for $FeMo_{0.80}V_{0.20}O_4$. The color-coding represents the assignment to different local Fe-sites, see text and Table 2. The dashed line indicates the crossover temperature.

around 200 K for α-$FeMoO_4$ has been observed.[11] Thus, we attribute this change in charge ordering to a phonon assisted process which is consistent with a polaronic scenario. The charge delocalization at high temperatures has an additional component, namely the Fe^{III} species (Sa) with vanishing QS. We relate the presence of such a narrowed singlet to fast charge fluctuations with a higher frequency than the spectral observation time of 10^{-8} s. Once the fluctuations slow down below 225 K, the charge appears localized on the time scale of the experiment ($Fe^{2+\delta}$, D3a) and the Fe^{III}-subspectrum (Sa) vanishes. The QS-value for D3a (≈1.0 mm/s at high temperatures) resembles an intermediate QS-value between Fe1 in α- and β-$FeMoO_4$. Presumably, this Fe1-site is located in the vicinity of a V-substitution, see also Figure 1. The site-percentage of 12(1)% (D3a subspectrum) furthermore corroborate the nominal V-substituted Mo1-sites (n = 0.11). The pure Fe^{II} sites (D1a and D2a) differ in their QS parameters and thereby clearly indicate the lifting of the degeneracy of the electric field gradients. This is due to the anisotropy originating from charge ordering effects that occur only on a single Fe-species (Fe1-site). In the high-temperature range the D2a-subspectrum vanishes, indicating that the EFG for all Fe^{II} species become equal and comparable to α-$FeMoO_4$.

The main difference between α-$FeMo_{0.89}V_{0.11}O_4$ with an exclusive V-substitution on Mo1-sites and α-$FeMo_{0.80}V_{0.20}O_4$ is the additional occupancy of Mo2-sites (edges of the Fe_4-tetramer), see Figure 1 and 4. Thereby, the structural asymmetry increases, which concomitantly alters the charge distribution. We observe four Fe-species in the Mössbauer spectra in the entire temperature range (Figure 7). The hyperfine parameters for the two Fe^{II}-species (D1b, blue and D2b, purple) follow approximately the same trend as described for x = 0.11 (D1a and D1b). The site percentages of these two amount overall to ≈60% at all temperatures. A third Fe^{II}-species (D4b, green) exhibits slightly larger CS- and distinct smaller QS-values, and compares well to Fe1 in β-$FeMoO_4$, see Table 2. This site contributes additionally ≈20% to the total Fe^{II}-fraction, leaving the remaining phase percentage to Fe^{III} (Sb, D3b, red) well in line with the nominal composition α-$FeMo_{0.80}V_{0.20}O_4$. Again, we observe the crossover from charge localization, as indicated by a non-vanishing QS for Fe^{III} (D3b), to a fast fluctuating Fe^{III}-species (Sb, charge-exchange narrowed singlet) around the phonon mediated transition temperature of 225 K. This change in charge distribution adds an anisotropy, which is reflected by the electric field gradients and alters the individual site-percentages of Fe^{II}-sites. The asymmetry originating from the V-substituted Mo2-sites (edges of the Fe_4-tetramer) reduces the site-percentage of D1b below 225 K and concomitantly increases the D2b and D4b fractions. Thus indicating that the latter two reveal additional information on the local structural distortion at Fe^{II}-sites upon charge trapping, see Figure 1. Note, contrary to $FeMo_{0.89}V_{0.11}O_4$ charge delocalization in $FeMo_{0.80}V_{0.20}O_4$ is reduced at all temperatures, compare D3a with D3b.

Conclusion

The synthesis of the mixed-valent solid solution series $FeMo_{1-n}V_nO_4$ is achieved by incorporating $FeVO_4$ in a metallothermic reaction of Fe and Fe_2O_3 in the presence of MoO_3. The latter solid-state reaction typically leads to the formation of $FeMoO_4$. It can be inferred that short reaction times and synthesis temperatures below the incongruent melting point of $FeVO_4$ prevents additional redox reactions involving vanadium. Such internal redox-reactions, reflecting the persisting gradient between Fe^{II} and vanadate and molybdate for the non-coexisting binary oxides in the thermodynamic limit, are absent in this solid solution series. The internal "chemical pressure" of the smaller cations (Fe^{III}, V^{V}) replacing Fe^{II} and Mo^{VI}, respectively, leads to increasing fractions of the low-temperature α-phase with increasing n. V-site preferences on the two Mo-positions differ for the two modifications. We observe a larger V-occupancy (≈0.3) exclusively on Mo1-positions in the β-phase. However, the accompanying molar volume reduction eventually induces the transformation into the more dense α-polymorph. Interestingly, the latter phase additionally exhibits different V-distributions involving also the Mo2-position for entropic reasons. Such disparate vanadium occupations of Mo-sites mark the differences in the charge localization / delocalisation: α-$FeMo_{0.89}V_{0.11}O_4$ (≈1/8 V-substitution on Mo1-positions) and α-$FeMo_{0.80}V_{0.20}O_4$ (V-substitution on Mo1- and Mo2-positions). In these hole-doped semiconducting materials, charge carriers (holes, Fe^{III}) delocalize via a hopping process assisted by electron-phonon interaction above 225 K as observed by

Mössbauer spectroscopy. In such a polaronic scenario, charge fluctuations (faster than the lifetime of an excited ^{57}Fe-nucleus) are enhanced for single Mo-site substitutions (case α-$FeMo_{0.89}V_{0.11}O_4$) and reduced by self-trapping once substitution of Mo2-positions is present. In principle, such a polaron should be magnetic and originate from direct exchange. We follow up on this aspect and present the magnetic properties of the $FeMo_{1-n}V_nO_4$ series in a forthcoming publication.

Experimental Section

Synthesis. The synthesis of $FeMoO_4$ was carried out starting from Fe_2O_3 (99,9% ChemPur, fine chemicals), MoO_3 (99,9+% ChemPur, fine chemicals) and Fe (99,9% ChemPur, fine chemicals, powder, d = 200 nm) in Ar purged and evacuated ($p \approx 2 \times 10^{-2}$ mbar) silica ampules at 700 °C (48 h) and for 24 h for reaction temperatures above ($750 \leq T \leq 900$ °C). Powder samples of $FeVO_4$ were prepared by solid state techniques from V_2O_5 (99,8%; ChemPur, fine chemicals) and Fe_2O_3. The starting materials were mixed in a 1:1 ratio, ground, placed into a corundum crucible and heated to 700 °C for 48 h. The cooled mixture was repeatedly ground, pressed into pellets and annealed for 24 h at 700 °C in air. Powder samples of the series, $FeMo_{1-n}V_nO_4$ were prepared using the respective molar ratios of Fe, MoO_3, Fe_2O_3 and $FeVO_4$. The mixtures were thoroughly ground, placed in previously purged silica tubes, which were then evacuated and sealed. The reaction temperature of the $FeMo_{1-n}V_nO_4$ series was 800 °C maintained for 24 h. A heating rate of 50 K/h and a cooling rate of 100 K/h were used for all reactions.

X-ray diffraction. The samples were characterized by Rietveld methods (TOPAS[39]) of x-ray diffraction data collected at room temperature on a STOE Stadi P powder diffractometer (STOE&Cie GmbH Darmstadt), using MoKα$_1$ radiation, Ge-(111) monochromator and a Dectris MYTHEN 1 K detector and polyvinyl acetate (PVAC) foils on a flat sample holder with external calibration (LaB_6 standard). Additionally, the lattice parameters for $FeMoO_4$ and the $FeMo_{1-n}V_nO_4$ substitution series were determined from capillary measurements (internal zero point correction). Considering the overall e.s.d.'s (typically 0.2%wt), the relative phase amounts of the α- and β-modification are reliable at the 1%wt level which is in the range that includes the end members of the series. Accordingly, one observes e.s.d.'s of the (Mo/V)-site occupation factors in the β-phase as high as 0.2, whereas in the α-modification these typically exceed the 10fold value of their corresponding e.s.d.'s. Therefore, we specify the values of n, x, and y by two significant digits. In-situ x-ray powder diffraction was performed with a STOE Stadi P powder diffractometer (STOE&Cie GmbH Darmstadt), using MoKα$_1$ radiation, Ge-(111) monochromator and two Dectris MYTHEN 1 K detectors in offset mode and a HT2 furnace (STOE&Cie GmbH Darmstadt). The powder samples were mounted in silica capillaries ($Ø_{outer} = 2$ mm, $Ø_{inner} = 1$ mm, Hilgenberg). Data was collected in a dry nitrogen flow (15 mL/min) at constant temperatures in steps of 25 °C between 25 °C and 525 °C upon heating and cooling (5 °C/min).

Thermal analysis. Differential scanning calorimetry (DSC) was performed on a DSC 3+ (Mettler Toledo) using sealed aluminum crucibles in a nitrogen flow of 20 mL/min. The sample masses ranged between 6.0 and 12.5 mg. The manufacturer's software (Mettler-Toledo, STARe Software V16.10) was used for data evaluation and calculation of enthalpies.

^{57}Fe-Mössbauer spectroscopy. ^{57}Fe-Mössbauer spectra were collected in transmission mode with a custom-built spectrometer using a ^{57}Co(Rh)-source in the temperature range from 40 to 300 K (closed cycle cryostat, C2 Montana Instruments). Typically, 25 mg of powdered sample was suspended in approx. 100 mg Paraffin (m.p. 42–44 °C) and the wax-like suspension was spread across a 16 mm diameter PE-disc. In order to eliminate texture effects we proceeded the measurements under the magic angle. Therefore, we mounted the sample with an angle of approx. 55(1)° between the normal vector of its basal plane and the wave vector (k_γ) of the incoming γ-photons. The Mössbauer spectrometer was calibrated with respect to α-iron foil at room temperature, which serves also as a reference for the isomer shift. Spectra were fitted by Lorentzian line-shape analysis as implemented in the Recoil software.[37]

DFT calculations were performed with the program package CASTEP 21.11[33] using the Perdew-Burke-Ernzerhof generalized gradient approximation for solids,[40] the built-in ultrasoft pseudopotentials, an energy cut-off of 1001.379 eV, and applying a Monkhorst-Pack *k*-point sampling of a 0.015 Å^{-1} spacing (80 *k*-points). The hypothetical ordered structure model was derived from the experimentally determined crystallographic data by generating non-reduced *2b*-superstructures.[41] These super-cell structures were decorated with 1/8 vanadium replacement on Mo1-sites and Mo2-sites, respectively. The electric field gradients EFG[34] given by V_{ii} tensors were computed without further relaxation of the structure models.

Acknowledgements

Funded by the Deutsche Forschungsgemeinschaft (DFG, German Research Foundation) Project-ID 443703006, CRC 1487. AM and VK acknowledge support from the Carl Zeiss Foundation. Parts of this research were conducted using the supercomputer MOGON 2 and/or advisory services offered by Johannes Gutenberg-University Mainz (hpc.uni-mainz.de), which is a member of the AHRP (Alliance for High Performance Computing in Rhineland-Palatinate, www.ahrp.info) and the Gauss Alliance e.V. The authors gratefully acknowledge the computing time granted on the supercomputer MOGON 2 at Johannes Gutenberg-University Mainz (hpc.uni-mainz.de). Open Access funding enabled and organized by Projekt DEAL.

Conflict of Interest

The authors declare no conflict of interest.

Data Availability Statement

The data that support the findings of this study are available from the corresponding author upon reasonable request.

Keywords: Solid Solution · Molybdate · Vanadate · ^{57}Fe-Mössbauer Spectroscopy · Thermal Analysis

[1] L. H. d. Lacerda, M. A. San-Miguel, *J. Mater. Sci.* **2022**, *57*, 10179–10196.
[2] S. K. Ray, J. Hur, *J. Environ. Manage.* **2021**, *278*, 111562.
[3] Y. Zhang, H. Mei, J. Yang, S. Wang, H. Gao, X. Jia, J. Yan, Y. Cao, Hw. Luo, K. Gao, *Ionics* **2020**, *26*, 3579–3590.

[4] K. Chu, Q. Li, Y. Cheng, Y-p. Liu, *ACS Appl. Mater. Interfaces* **2020**, *12*, 11789–11796.
[5] M. Minakshi, T. Watcharatharapong, S. Chakraborty, R. Ahuja, *APL Mater.* **2018**, *6*, 047701.
[6] V. Blanco-Gutierrez, A. Demourgues, O. Toulemonde, A. Wattiaux, O. Nguyen, M. Gaudon, *Inorg. Chem.* **2015**, *54*, 2176–2184.
[7] L. Righetti, L. Robertson, A. Largeteau, G. Vignoles, A. Demourgues, M. Gaudon, *Appl. Mater. Interf.* **2011**, *3*, 1319–1324.
[8] J. A. Rodriguez, J. C. Hanson, S. Chaturvedi, A. Maiti, J. L. Brito, *J. Phys. Chem. B* **2000**, *104*, 8145–8152.
[9] A. W. Sleight, B. L. Chamberland, *Inorg. Chem.* **1968**, *8*, 1672–1675.
[10] A. W. Sleight, B. L. Chamberland, J. F. Weiher, *Inorg. Chem.* **1968**, *7*, 1093–1098.
[11] V. Ksenofontov, Y. G. Pashkevich, M. Panthöfer, V. Gnezdilov, R. Babkin, R. Klauer, P. Lemmens, A. Möller, *J. Phys. Chem. C.* **2021**, *125*, 5947–5956.
[12] R. A. M. Ram, J. Gopalakrishnan, *J. Chem. Sci.* **1986**, *96*, 291–296.
[13] H. Ehrenberg, G. Wltschek, F. Trouw, T. Kroener, H. Weitzel, H. Fuess, *J. Magn. Magn. Mater.* **1994**, *135*, 355–360.
[14] L. Vegard, *Z. Phys.* **1921**, *5*, 17–26.
[15] Y. Laligant, L. Permer, A. Le Bail, *Eur. J. Solid State Inorg. Chem.* **1995**, *32*, 325–334.
[16] A. Le Bail, L. Permer, Y. Laligant, *Eur. J. Solid State Inorg. Chem.* **1995**, *32*, 883–892.
[17] J. Walczak, M. Kurzawa, T. L. Trześniowska, *Thermochim. Acta.* **1985**, *92*, 567–570.
[18] X. Wang, K. R. Heier, C. L. Stern, K. R. Poeppelmeier, *Inorg. Chem.* **1998**, *37*, 6921–6927.
[19] T. Groń, J. Krok-Kowalski, M. Kurzawa, J. Walzak, *J. Magn. Magn. Mater.* **1991**, *101*, 148–150.
[20] a) S. Lopez-Moreno, D. Errandonea, J. Pellicer-Porres, D. Martinez-Garcia, S. J. Patwe, S. N. Achary, A. K. Tyagi, P. Rodriguez-Hernandez, A. Muñoz, C. Popescu, *Inorg. Chem.* **2018**, *57*, 7860–7876; b) J. Gonzalez-Platas, S. Lopez-Moreno, E. Bandiello, M. Bettinelli, D. Errandonea, *Inorg. Chem.* **2020**, *59*, 6623–6630.
[21] P. Schmidt, *Habilitationsschrift*, TU Dresden **2007**.
[22] C. Gleitzer, J. B. Goodenough, *J. Mater. Sci. Lett.* **1987**, *6*, 939–941.
[23] Y. P. Yadava, R. A. Singh, *J. Mater. Sci.* **1986**, *21*, 2825–2829.
[24] N. Suresh Rao, O. G. Palanna, *Bull. Mater. Sci.* **1995**, *18*, 229–236.
[25] A. Dixit, P. Chen, G. Lawes, J. L. Musfeldt, *Appl. Phys. Lett.* **2011**, *99*, 141908.
[26] A. Dixit, G. Lawes, *J. Phys. Condens. Matter.* **2009**, *21*, 456003.
[27] M. Sorescu, T. Xu, J. D. Burnett, J. A. Aitken, *J. Magn. Magn. Mater.* **2015**, *387*, 37–45.
[28] V. D. Nithya, R. K. Selvan, *Phys. B* **2011**, *406*, 24–29.
[29] K. Zaghib, A. Mauger, J. B. Goodenough, F. Gendron, C. M. Julien, *Chem. Mater.* **2007**, *19*, 3740–3747.
[30] C. Franchini, M. Reticcioli, M. Setvin, M. U. Diebold, *Nat. Rev. Mater.* **2021**, *6*, 560–586.
[31] R. D. Shannon, *Acta Crystallogr.* **1976**, *A32*, 751–767.
[32] R. Hübenthal, R. Hoppe, *MAPLE, Program for the Calculation of the Madelung Part of Lattice Energy*, University of Gießen **1993**.
[33] S. J. Clark, M. D. Segall, C. J. Pickard, P. J. Hasnip, M. J. Probert, K. Refson, M. C. Payne, *Z. Kristallogr.* **2005**, *220*, 567–570.
[34] M. Profeta, C. J. Pickard, F. Mauri, *J. Am. Chem. Soc.* **2003**, *125*, 541–548.
[35] N. N. Greenwood, T. C. Gibbs, *Mössbauer Spectroscopy*, Chapman and Hall Ltd., London 1971.
[36] M. Pápai, G. Vankó, *J. Chem. Theory Comput.* **2013**, *9*, 5004–5020.
[37] K. Lagarec, D. G. Rancourt, *Recoil – Mössbauer spectral analysis software for Windows V1.0*, University of Ottawa, Canada **1998**.
[38] P. D. Battle, A. K. Cheetham, G. J. Long, G. Longworth, *Inorg. Chem.* **1982**, *21*, 4223–4228.
[39] A. A. Coelho, TOPAS-Academic-64 V7.14; Topas **2020**.
[40] J. P. Perdew, A. Ruzsinszky, G. I. Csonka, O. A. Vydrov, G. E. Scuseria, L. A. Constantin, X. Zhou, K. Burke, *Phys. Rev. Lett.* **2008**, *100*, 136406.
[41] T. Björkman, *Comput. Phys. Commun.* **2011**, *182*, 1183–1186.

Manuscript received: August 21, 2022
Revised manuscript received: September 15, 2022
Accepted manuscript online: September 16, 2022

